Nanoscale glass cold welding

Yunna Guo,[1,5] Hantao Cui,[1,5] Peng Jia,[1] Zhangran Ye,[1] Lei Deng,[1] Hui Li,[1] Baiyu Guo,[1] Xuedong Zhang,[2] Jie Huang,[4] Yong Su,[2] Jianyu Huang,[1,2] Bin Wen,[4,*] Yang Lu,[3,6,*] and Liqiang Zhang[1,*]

[1] Clean Nano Energy Center, State Key Laboratory of Metastable Materials Science and Technology, Yanshan University, Qinhuangdao 066004, P. R. China

[2] Key Laboratory of Low Dimensional Materials and Application Technology of Ministry of Education, School of Materials Science and Engineering, Xiangtan University, Xiangtan, Hunan 411105, P. R. China

[3] Department of Mechanical Engineering, The University of Hong Kong, Hong Kong, P. R. China

[4] Center for Extreme Deformation Research, State Key Laboratory of Metastable Materials Science and Technology, Yanshan University, Qinhuangdao 066004, P. R. China

[5] These authors contributed equally

[6] Lead contact

* Correspondence:

wenbin@ysu.edu.cn (B.W.),

ylu1@hku.hk (Y.L.),

lqzhang@ysu.edu.cn (L.Z.)

SUMMARY

Bottom-up assembly and joining of silica nanoparticles to form complicated geometries up to three-dimensional (3D) glass structures are attractive for nanoscale optical, optoelectronics, etc. Most existing silica 3D printing techniques can only achieve submicron-level precision due to the optical limit of vat photopolymerization, which presents critical challenges for sub-100 nm printing. In this context, we introduce an electron beam-assisted cold welding technique for nanoscale glass, that is capable of achieving precision at the tens-of-nanometers scale. This method enables the direct fusion of two amorphous silica nanospheres within a few seconds while keeping the diameter smaller than 100 nm. Meanwhile, the strength, composition, and structure of the as-welded junctions appear the same as the pristine silica. Our approach would potentially allow ultrahigh-resolution 3D bottom-up assembly and printing of silica nanostructures with ultimate resolution subject to the nanoparticle size only, which offers a new approach for additive manufacturing of nanoscale glass devices.

INTRODUCTION

Amorphous SiO_2 (Silica glass) possesses excellent optical transparency, thermal stability, chemical stability, and good mechanical properties, making it one of the most important materials in modern engineering applications.[1] With its wide application in areas such as micro-optics, nanofluidics, nanophotonics, and other nanoelectromechanical systems,[2-4] there is a growing demand for the processing of nano-sized glass. Although various glass processing techniques such as 2D mask lithography, thermal oxidation, three-dimensional lithography, direct ink writing, and digital light processing have been developed,[5] these processes are hard to achieve a resolution of below 200 nm.[6-8] The main reason is that the traditional technology relies on the melting of the precursor,[9,10] which inevitably cause the serious agglomeration of silica, and greatly reduces the precision of welding. To avoid these drawbacks, achieving rapid cold welding of nano-sized silica is a good choice for 3D printing amorphous glass technology, however, this is a significant challenge to date.[9] Herein, facile cold welding of ceramic amorphous silica was achieved in the advanced Cs image-corrected environmental transmission electron microscope (ETEM). Under the electron beam (e-

beam) irradiation, an ultra-clean surface was obtained. Meanwhile, the ductility of silica is enhanced. As a result, two contacted amorphous silica nanospheres can be firmly welded together in several seconds, based on this basic operation, even a complex structure can be assembled.

RESULTS AND DISCUSSION

In situ e-beam assisted cold welding of silica nanospheres in an ETEM

The welding process of silica nanospheres was performed by using a TEM-scanning tunneling microscope (TEM-STM, Pico-Femto) platform in a Cs-corrected FEI Titan ETEM G2 (Figure S1A). The silica nanospheres with an average diameter of 100 nm were bought from Guangdong Meigu Chemical Co., Ltd (Metasil ML-100) (Figure S2). The welding process is shown schematically in Figure 1A. Many silica nanospheres were firmly attached to the edge of a copper mesh through the electrostatic force (Figure S1B). The tungsten (W) tip prepared for welding the silica nanosphere was obtained by a typical electrochemical corrosion method (Figure S3). Prior to the experiment, we pre-coated a layer of silica (20 nm) onto the surface of the W tip by using a physical vapor deposition (PVD) technique. After that treatment, the cold welding of W tip with the first silica becomes quite easy. In the experiment, the W tip was slowly moved to touch the surface of silica nanosphere (Figures 1B–1D). And then, we then magnified the weld junction to 620× kx, resulting in a high dose of e-beam (~6.94 A/cm^2) showering on the weld junction. After 10 s, the W tip and silica nanosphere were welded together. After that, we immediately reduced the magnification to 34× kx. Meanwhile, the e-beam intensity was sharply reduced to ~3.02×10^{-2} A/cm^2, after which the 1st welding was established (Video S1).

After the 1st welding, we pulled the W tip backward and found that the silica nanosphere already welded to the W tip could be separated from the loose silica nanosphere on the left side (Figure 1D). After the first welding, there is no influence on the material, and the welded silica can continue to be welded. Thus, another silica nanosphere was welded onto the first one by using the same technique (2nd welding; Figures 1E and 1F). When the 2nd welding process was finished, we also quickly pulled the W tip backward. It was found that the first and second nanosphere were firmly welded together, and they could be separated from the other unwelded nanospheres

(Figure 1F), this indicating the good strength of the weld junction. Following the same welding procedure, the 3rd, 4th, 5th, 6th, and 7th were welded, forming a silica nanosphere chain (Figures 1G–1K and S4; Video S2).

For each welding procedure, when the two silica nanospheres come into contact, their surfaces rapidly adhere and extend, this process is completed in about 222 s (Figures 2A – 2D). Dependent on the stacking order of silica nanospheres, many complex three-dimensional (3D) shapes and device can be constructed (Figures 1L–1O and S5), which confirms the feasibility of this method. Even without applying any extra stress, we observed that the silica nanospheres could also be automatically welded together (Figure S6), indicating its potential application in 3D printing. The mechanism was believed to be associated with surface-diffusion-mediated pseudoelastic deformation at room temperature, which was driven by the extra driving force from capillary-energy minimization.[11]

The corresponding Fast Fourier Transform (FFT) image indicates that the welding junction area and the original silica were both in an amorphous state (Figures S7A–S7E), Electron energy loss spectroscopy (EELS) analysis also confirms the welding junction still maintained the same as the pristine silica (Figures S7F and S8), and there were no changes in valence state or composition during the welding process.[12] To evaluate the mechanical properties of this weld junction, a self-assembled in situ TEM-atomic force microscopy (AFM) device is set up,[13] as illustrated in Figures 2E and 2F. Firstly, several silica nanospheres were welded onto the tip of a silicon substrate, and then we welded the top silica nanosphere onto the AFM cantilever. As the initial welding completed, the diameters of the fused silica nanospheres will become more and more uniform, and eventually become a solid rod structure. Under the tensile force, the welded silica nanospheres move downwards, meanwhile the AFM cantilever was bent (Figure 2E). After stretching 370 nm, the welded silica nanospheres broke in the medial and the fracture surface displayed a brittle fracture characteristic (Figures 2G–2J and Video S3). According to the formula: $F=K\cdot\Delta X$, $P=F/S$, $S=\pi d^2/4$, where F is the force, K is the force constant, ΔX is the displacement of the AFM cantilever, and S is the fracture area of the silica nanorod, d is the diameter of the fracture surface. In Figures 2E-J, K=6 N/m, ΔX=370 nm, d=114 nm. As a result, we can calculate that the tensile strength of the weld junction reached as high as 217 MPa. To ensure the reliability of

the data, we re-tested several tensile mechanical properties of the welded silica. It was found that the calculated average tensile strength of the weld junction falls in the range of 185~217 MPa, which is equivalent to the tensile strength of macroscopic silica materials.[14]

Control of welding process via surface modification

As we know, welding is closely related to the surface state of the material. There are different gases (including no gas, CHF_3-SF_6-O_2, and H_2) introduced into the ETEM chamber, and the corresponding welding speeds (it is defined by the increase in contact area and time between two silica nanospheres) were measured, and they are plotted in Figures 3A–3C. In no gas environment, as shown in Figure 3A, the two silica nanospheres were welded together in a short time (154 s), and the welding speed of silica spheres is 0.16 nm/s. Under the CHF_3-SF_6-O_2 environment (Figure 3B), it was found that the silica sample displayed a much higher welding speed (2.64 nm/s). In previous study, it has been reported that the CHF_3-SF_6-O_2 gas is a typical etching gas for etching the silica.[15,16] CHF_3 and SF_6 were activated into F*, and silica was corroded under high-energy e-beam irradiation (Figure S9). Due to the generation of F*, the passivation layer located on the surface of silica could be removed. In comparison, the silica sample under H_2 environment displayed the slowest welding speed (0.04 nm/s) (Figure 3C and Video S4).

To rationalize this result, first-principle calculations (Computational method for interaction stress) were performed. It is found that when two silica nanospheres with different surface terminated states are gradually approaching each other, significantly different interaction stresses are produced between them (Figure 3D). For the silica without any hydrogen passivation on the surface, many dangling bonds exist. When these two silica nanospheres are gradually connected, their interaction stress is attractive (the red line in Figure 3D). With the decrease in their distance, their attractive stress increases as well. When the distance is less than 1 Å, the attractive stress can reach 10.4 GPa, this huge attracting stress between the silica surfaces can spontaneously achieve welding. While for the silica with a full hydrogen passivation surface, the interaction stress is quite different. When the two silica nanospheres approach each other, their interaction stress is repulsive (the black line in Figure 3D). When the distance is less than 0.5 Å, the repulsive stress can reach 2.0 GPa, which means that it

becomes extremely difficult for the materials to be welded (Figure S10 and Table S1).

Both experimental and computational results confirm that it is indeed hydrogen passivation that leads to the difficulty of welding. The hydrogen passivation level may determine the welding difficulty. To rationalize this idea, the surface energies for silica with different hydrogen coverage levels are calculated by using the first-principle method (Computational method for surface energy), which are plotted in Figure 3E. When the silica surface is completely terminated by hydrogen atoms (full hydrogen passivation), their surface energy is 1.22 J/m^2. When the hydrogen coverage rate decreases to 2/3, 1/3, the calculated surface energies of silica increase to 2.10 and 2.84 J/m^2, respectively. When the surface of silica is free of hydrogen coverage, resulting in a further increase in the surface energy of silica to 3.23 J/m^2 (Table S2). High surface energy means high surface tension and high chemical reactivity. It indicates that the silica after CHF_3-SF_6-O_2 treatment possesses an ultra-clean surface, which has a high chemical reactivity and provides a high driving force to lower the energy barrier for plastic deformation, and this is beneficial for the welding process. These results indicate that the cold welding speed of ceramic silica can be easily adjusted by controlling the gas, which is crucial for future 3D printing.

The e-beam assisted cold welding mechanism

The deformation ability of ceramic materials is closely related to the concentration of defects, which has a close relationship with the intensity of e-beam irradiation.[17] Thus, the mechanical properties of silica nanosphere under e-beam on/off conditions are explored respectively. Electrons have much greater penetration depths compared to heavier particles and ions, so they can generate uniform damage and structural changes throughout a material. The principle of the in situ mechanical testing technique is to compress individual silica nanosphere between a flat diamond punch and a flat silicon substrate while simultaneously observing the deformation process. Figure 4A shows a typical stress-strain response of amorphous silica nanospheres in compression tests inside the ETEM by using a Hysitron Picoindenter (PI 95). Figure 4A chart the load-displacement curves and deformation behavior of the silica nanospheres before (inset) and after the experiments with beam-off and beam-on conditions. When the e-beam was off, the maximum average contact pressure on the sphere was approximately 97 μN just after ~50% compression. Alternatively, the effective stress on the nanospherical shell can be defined as the load divided by the initial maximal cross-sectional area of

the nanospherical shell.[18] This results in an effective yield strength of 9.26 GPa. In contrast, a much easier flow was observed when the e-beam was on during the in situ deformation experiments (Figure 4A). It yields an approximate effective yield strength at only 4.78 GPa. This unusual strength decrease enables the silica nanosphere to exhibit considerable plastic deformation to failure.

The electron-beam-induced defects including vacancies, and dangling bonds are interpreted as the direct reason for the observed soften effect.[19] Thus, the e-beam density plays a significant role for influence the welding speed of silica nanospheres (Figure S11). Under high-energy e-beam irradiation, the welding speed is 2.13 nm/s. Under moderate intensity e-beam irradiation, the welding speed is 1.64 nm/s. Under a low intensity e-beam irradiation, the welding speed is 0.26 nm/s. It indicates that the higher the e-beam dose, the faster the welding speed. However, the dose rate of the e-beam during welding process is not sufficient to cause a sharp increase in the sample temperature.[17,20] For a welding process, two steps are needed, the first step is the contact of welding interfaces, and the next step is the bonding between interface atoms. For the first step, the contact of welding interfaces needs large geometry changes or deformation, and this deformation is carried by atomic diffusion with the aid of vacancy. For the second step, the atoms on the interfaces have an unsaturated dangling bond, when two Si and O atoms with an unsaturated dangling bond reach a critical distance, these two atoms can be bonded. The broken/suspended bonds interacted with other neighboring atoms, accompanying the rotation and migration of the atomic clusters are also involved.[21] The repetition and accumulation of such bond-switching events cause plastic flow in the silica, healing incipient voids before their coalescence and giving rise to the observed ductility.

To further clarify this deformation mechanism, the welding time to reach constant silica nanospheres' contact width as a function of the reciprocal of temperature is summarized in Figure 4B. With increasing the temperature, the welding speed is enhanced as well, indicating that the deformation of silica is primarily driven by thermal activation. Usually, the strain rate/welding speed R in a thermal activation deformation process can be well described by Arrhenius equation[22]

$$R = A \exp\left(-\mathrm{G}/kT\right), \tag{1}$$

where A is a preexponential factor, and it is proportional to the concentration of the

deformation carrier (such as vacancy point defect); k is the Boltzmann constant; T is the temperature; G is the thermal activation energy barrier.

By linear fitting the logarithm of welding time as a function of the reciprocal of temperature (Figure 4B), the thermal activation energy barrier for this welding process can be obtained. For different welding progress, their thermal activation energy barriers are almost the same, which is in the range of 0.043~0.046 eV (according to equation 1; Table S3). For amorphous silica, its plastic deformation is dominated by atomic diffusion, hence their thermal activation energy barriers correspond to the atomic diffusion barrier. Under no external applied stress condition, the atomic diffusion barrier usually is in the range of 0.4~0.6 eV.[23] This result implies that the micro mechanism of our welding process is a stress-derived atomic diffusion process, and the surface tension force played the role of external applied stress to drive the atomic diffusion process. This surface tension is originated from the spherical structure of silica, which is closely related to its diameter.

In our cold welding process, the deformation carrier is mainly vacancy point defects (it is proportional to the A in Eq. 1), and it may be caused by e-beam irradiation.[17,24,25] As shown in Eq.1, the increase in the concentration of defect A can accelerate the welding speed, this explains why the amorphous silica under e-beam irradiation displays a lower strength than that without irradiation. Based on the above analysis, the welding mechanism of ceramic silica can be concluded as a combined thermal and mechanical activation mechanism, and this mechanism to overcome the energy barrier for a plastic deformation process is schematically illustrated in Figure 4C.

CONCLUSIONS

In this study, a silica cold welding technology with an accuracy at the tens-of-nanometers scale is achieved under e-beam irradiation. A clean surface and high plastic deformation ability are two critical factors for achieving room temperature welding of silica. When the hydrogen passivation layer is cleaned up, more newly formed free bindings are likely to be accumulated on the surface, resulting in the easier welding of silica at room-temperature. Not only alters the surface state, e-beam irradiation created plenty of defects through ionization and excitation of atoms inside the silica, which

significantly improved its plastic deformation ability. Therefore, we can control the welding speed of silica by controlling the electron beam and atmosphere environment.

Although cold welding is a well-known phenomenon in metal, its occurrence in ceramic material under an ambient atmosphere is unexpected. Moreover, the welding process is automatically carried out without needing any extra stress. From a scientific perspective, the current study not only spatiotemporally tracks the cold welding process of ceramic material, but also provides direct evidence that hydrogen passivation layer can significantly influence the welding speed. In application wise, this unique glass cold welding technique has many characteristics including flexibly control, low temperature, and strong welding strength, maximally retaining the excellent properties of silica itself but without disturbing its nano scale resolution (even down to sub-10 nm depending on the nanoparticle sizes). This method demonstrated silica can be facilely processed with an ultra-high resolution below 100 nm, revealing the potential to build passive and active integrated nanophotonic chips and glass devices via direct 3D nanoprinting.

EXPERIMENTAL PROCEDURES

Resource availability

Lead contact

Further information and requests for resources and data should be directed to and will be fulfilled by the lead contact, Yang Lu (ylu1@hku.hk).

Materials availability

This study did not generate new unique reagents.

Data and code availability

All the necessary data supporting the main findings of the paper are available within the main paper and its supplemental information files and from the lead contact upon reasonable request.

The setup of the cold welding

The welding processes of silica nanospheres were carried out in a Cs-corrected FEI Titan ETEM G2 by using a TEM scanning tunneling microscope platform (PicoFemto, STM-TEM holder).[13,26] The three-dimensional motion of the STM probe is driven by the piezoelectric head of the stent. Prior to the experiment, a semicircular copper mesh was swept back and forth through the silica nanosphere powder. As a result, some silica nanospheres are adsorbed on the string of the semicircular copper mesh through an electrostatic force. And then, we use blowgun to remove excess loosely samples from the copper mesh. In this study, the in situ TEM characterization is carried out at room temperature. A slow scan CCD camera is used to record images and movies. The welding behavior of silica nanospheres is monitored under controlled electron irradiation and usual imaging conditions.

Description of the in situ tensile experiment

In order to quantitatively measure the tensile properties of the weld junction, we inserted a silicon atomic force microscopy (AFM) cantilever beam (k = 0.1~40 N/m) into one end of the environmental transmission electron microscopy – AFM (ETEM-AFM) holder. Silica nanospheres were used to connect the Si substrate tip to the cantilever under electron beam irradiation. In this welding process, we choose Si substrate instead of W because Si is a brittle material, and the plastic deformation will not occur during the stretching process, which ensures the reliability of the experiment. Because the deflection of the cantilever (< 5 μm) was much smaller than its beam length (520 μm), a linear relationship between Δx (displacement of the AFM tip, which is equal to the cantilever deflection) and P (force applied on the target silica sample) was assumed. During the experiment, a beam stopper was inserted into the field of view as the reference for displacement measurements. The compression strength was calculated from the engineering stress. The stress calculation was accurate by measuring cantilever deflections in high-magnification TEM images.

Tuning the surface conditions on the welding process

Numerous works in literatures have reported that there are dangling bonds on the surface of any materials,[27-29] it affects the surface state of silica. A typical phenomenon is called hydrogen passivation.[30,31] In the experiment, the two contacted silica

nanospheres could not be welded together under H_2 atmosphere.

The CHF_3-SF_6-O_2 gas is a typical etching gas widely used in the semiconductor industry, especially for etching the silica.[15,16] As already reported in a previous study,[32,33] the chemical reaction between silica and CHF_3-SF_6-O_2 is the reaction between silica and reactive fluorine generates volatile SiFx. Firstly, CHF_3 was activated into F* and the gas became extremely active under electronic irradiation. The chemical reactions between silica and F* caused the breaking of chemical bonds.[34] As a result, the impurity atoms located on the surface of silica could be removed, and an ultra-clean silica surface was formed after CHF_3-SF_6-O_2 gas treatment.

In comparison, the silica sample under H_2 environment is expected to own a full hydrogen-terminated surface. In the experiment, the surface of the pristine silica nanosphere was first cleaned up by using CHF_3-SF_6-O_2 gas, resulting in exposing more dangling bonds. After that, the CHF_3-SF_6-O_2 gas was pumped out from the ETEM chamber. Subsequently, 0.01 mbar H_2 (99.999% purity) was introduced into the chamber. Under e-beam irradiation, H_2 gas molecules were easily ionized. A large number of free hydrogen atoms or ions were generated at this time, which could easily terminate the dangling bonds on the fresh silica nanosphere surface and form a full hydrogen-terminated surface.

Parameter setup for first principle calculation

For both enthalpies of formation and surface energy calculations, their first-principles energy calculations are performed by using the Vienna ab initio simulation package (VASP) based on density functional theory (DFT).[35,36] Based on the models built above, they are relaxed firstly, and then the corresponding total energy be obtained by first-principles energy calculation. In this work, the required elements are calculated by using projector augmented wave (PAW) pseudopotential.[37] The generalized gradient approximation (GGA) in the form of Perdew-Burke-Ernzerhof (PBE).[38] The cut-off energy of plane-wave is set at 500 eV, and only one k-point of Gamma is used.

Computational method for interaction stress

To study the welding mechanism, the interaction stresses of two amorphous silica surfaces are studied by using first-principle method. To simulate this situation, a serial

of slab structure models with different vacuum layers thickness are established, as shown in Figure S10. Because it is a slab model, the vacuum layers thickness can represent the contact distance L. In these slab models, 55 silicon atoms and 110 oxygen atoms are contained, and there exist two types of surfaces, one is the surface without any hydrogen passivation, and the other one is the surface with a full hydrogen-terminated.

The enthalpies of formation as a function of contact distance L is calculated by using the following formula:

$$\Delta H(L) = 1/2(H_L - H_\infty), \quad (1)$$

where H_L is the system enthalpy when the contact distance is L, and H_∞ is the enthalpy value at infinity, in this work, the H_∞ is take as the system enthalpy value at the contact distance L = 15 Å. After that, the enthalpy of formation is differentiated by the contact distance and further divided by the contact area, and it is the interaction stress, and they are listed in Table S1.

Computational method for surface energy

To study the surface state of amorphous silica surface, the surface energy of amorphous silica is calculated by using first-principle method. For calculating, a serial of slab structure models are established, and their vacuum layers thickness is selected as 15 Å to ensure two surfaces no interaction. In these slab models, 55 silicon atoms and 110 oxygen atoms are contained, and their surface are terminated with different coverage of hydrogen to simulate different experimentally treated surfaces. The hydrogen coverage rates are 0, 1/3, 2/3, and 1 respectively, as shown in Table S2.

The surface energy as a function of hydrogen chemical potential is obtained by using the following formula:

$$E_{surface} = (E_{slab} - N * E_{bulk} - n * \mu_H)/2A, \quad (2)$$

where E_{slab} is the total energy of slab composed of N-layer bulks, E_{bulk} is the energy of the bulk, A is the surface area of the slab, and n is the amount of surface terminated hydrogen, μ_H is the hydrogen chemical potential. $\mu_H = E_{H_2}/2$, E_{H_2} is the total energy of dissociating and isolating a hydrogen molecule at T=0 K.

Finally, the calculated Surface energy can be obtained, and they are listed in Table S2.

ACKNOWLEDGMENTS

L.Z., J.H. and B.W. acknowledge funding under the National Natural Science Foundation of China (Nos. 52022088, 51971245, 51925105, U23A20537). L.Z. acknowledges support from funding by S&T Program of Hebei (B2023203037). L.Z. acknowledges support funding from Science Research Project of Hebei Education Department (JZX2024022). L.Z. acknowledges support funding from Natural Science Foundation of Hebei Province (Nos. F2021203097, B2024203054). The authors acknowledge support from the Department of Mechanical Engineering, The University of Hong Kong. Y.L. acknowledges support funding from Research Grants Council of the Hong Kong Special Administrative Region, China under grant RFS2021-1S05, and Innovation and Technology Fund (ITF) project under GHP/221/21GD.

AUTHOR CONTRIBUTIONS

Y.G. and L.Z. conceived and designed the project. P.J., Z.Y. and L.D. fabricated the samples. Y.G. H.L. and B.G. carried out the in situ ETEM experiments. H.C and J.H. performed computational modeling. Y.L. B.W. and L.Z. supervised the experiments. Y.G., Y.L. and L.Z. co-wrote the paper. All the authors discussed the results and commented on the manuscript.

DECLARATION OF INTERESTS

The authors declare no conflict of interest.

REFERENCES

1. Colombo, P. & Franchin, G. (2023). Improving glass nanostructure fabrication. Science 380, 895-896. https://doi.org/10.1126/science.adi2747.
2. Wang, B. J., Han, Y., Xu, S., Qiu, L., Ding, F., Lou, J. & Lu, Y. (2018). Mechanically assisted self-healing of ultrathin gold nanowires. Small 14, 1704085. https://doi.org/10.1002/smll.201704085.
3. Liu, Y. X., Lu, Y. & Tu, K. N. (2022). Low temperature interfacial reaction in 3D IC nanoscale materials. Mat. Sci. Eng. R 151, 100701. https://doi.org/10.1016/j.mser.2022.100701.
4. Du, X. T., Xu, Y., Liu, H., Li, Z. L., Zhu, L. M. & Zhu, Z. W. (2023). Precise and Rapid Replication of Complex-Shaped Fused Silica Optics. Adv. Opt. Mater. 11, 2300840. https://doi.org/10.1002/adom.202300840.
5. Kotz, F., Quick, A. S., Risch, P., Martin, T., Hoose, T., Thiel, M., Helmer, D. & Rapp, B. E. (2021). Two-Photon Polymerization of Nanocomposites for the Fabrication of Transparent Fused Silica Glass Microstructures. Adv. Mater. 33, 2006341. https://doi.org/10.1002/adma.202006341.
6. Wen, X. W., Zhang, B. Y., Wang, W. P., Ye, F., Yue, S., Guo, H., Gao, G. H., Zhao, Y. S., Fang, Q. Y., Nguyen, C. *et al.* (2021). 3D-printed silica with nanoscale resolution. Nat. Mater. 20, 1506-1511. https://doi.org/10.1038/s41563-021-01111-2.
7. Hong, Z. H., Ye, P. A. R., Loy, D. A. & Liang, R. G. (2021). Three-dimensional printing of glass micro-optics. Optica 8, 904-910. https://doi.org/10.1364/optica.422955.
8. Bauer, J., Crook, C. & Baldacchini, T. (2023). A sinterless, low-temperature route to 3D print nanoscale optical-grade glass. Science 380, 960-966. https://doi.org/10.1126/science.abq3037.
9. Tang, H., Cheng, Y., Yuan, X. H., Zhang, K., Kurnosov, A., Chen, Z., Xiao, W. E., Jeppesen, H. S., Etter, M., Liang, T. *et al.* (2023). Toughening oxide glasses through paracrystallization. Nat. Mater. 22, 1189-1195. https://doi.org/10.1038/s41563-023-01625-x.
10. Im, J., Liu, Y., Hu, Q., Trindade, G. F., Parmenter, C., Fay, M., He, Y. F., Irvine, D. J., Tuck, C., Wildman, R. D. *et al.* (2023). Strategies for Integrating Metal Nanoparticles with Two-Photon Polymerization Process: Toward High Resolution Functional Additive Manufacturing. Adv. Funct. Mater. 33, 2211920. https://doi.org/10.1002/adfm.202211920.
11. Xu, S., Li, P. & Lu, Y. (2017). In situ atomic-scale analysis of Rayleigh instability in ultrathin gold nanowires. Nano Res. 11, 625-632. https://doi.org/10.1007/s12274-017-1667-3.
12. Cheng, S. C., Song, C. Y. & Ercius, P. (2020). Electron energy loss spectra from silica glass optical fibers. J. Am. Ceram. Soc. 103, 4983-4988. https://doi.org/10.1111/jace.17200.
13. Zhang, L. Q., Tang, Y. S., Peng, Q. M., Yang, T. T., Liu, Q. N., Wang, Y. C., Li, Y. F., Du, C. C., Sun, Y., Cui, L. S. *et al.* (2018). Ceramic nanowelding. Nat. Commun. 9, 96. https://doi.org/10.1038/s41467-017-02590-1.
14. Callisterjr, W. D. (2018). *Materials science and engineering : an introduction*, 10th edn. (Wiley).
15. Lee, J., Lee, J., Lee, H. W. & Kwon, K.-H. (2015). Anti-adhesive characteristics of CHF_3/O_2 and C_4F_8/O_2 plasma-modified silicon molds for nanoimprint lithography. Mater. Res. Bull. 69, 120-125. https://doi.org/10.1016/j.materresbull.2014.12.023.
16. Knizikevičius, R. (2009). Simulations of Si and SiO_2 etching in SF_6+O_2 plasma. Vacuum 83, 953-957. https://doi.org/10.1016/j.vacuum.2008.11.002.
17. Zheng, K., Wang, C., Cheng, Y.-Q., Yue, Y., Han, X., Zhang, Z., Shan, Z., Mao, S. X., Ye, M., Yin, Y. *et al.* (2010). Electron-beam-assisted superplastic shaping of nanoscale amorphous

silica. Nat. Commun. 1, 24. https://doi.org/10.1038/ncomms1021.

18. Shan, Z. W., Adesso, G., Cabot, A., Sherburne, M. P., Syed Asif, S. A., Warren, O. L., Chrzan, D. C., Minor, A. M. & Alivisatos, A. P. (2008). Ultrahigh stress and strain in hierarchically structured hollow nanoparticles. Nat. Mater. 7, 947-952. https://doi.org/10.1038/nmat2295.

19. Mačković, M., Niekiel, F., Wondraczek, L. & Spiecker, E. (2014). Direct observation of electron-beam-induced densification and hardening of silica nanoballs by in situ transmission electron microscopy and finite element method simulations. Acta Mater. 79, 363-373. https://doi.org/10.1016/j.actamat.2014.05.046.

20. Yokota, T., Murayama, M. & Howe, J. M. (2003). In situ Transmission-Electron-Microscopy Investigation of Melting in Submicron Al-Si Alloy Particles under Electron-Beam Irradiation. Phys. Rev. Lett. 91, 265504. https://doi.org/10.1103/PhysRevLett.91.265504.

21. Romeis, S., Paul, J., Herre, P., de Ligny, D., Schmidt, J. & Peukert, W. (2015). Local densification of a single micron sized silica sphere by uniaxial compression. Scr. Mater. 108, 84-87. https://doi.org/10.1016/j.scriptamat.2015.06.023.

22. Argon, A. (2007). *Strengthening Mechanisms in Crystal Plasticity*. (Oxford University Press).

23. Kuo, C.-L., Lee, S. & Hwang, G. S. (2008). Structure and dynamics of silicon-oxygen pairs and their role in silicon self-diffusion in amorphous silica. J. Appl. Phys. 104, 054906. https://doi.org/10.1063/1.2974757.

24. Chen, Y.-C., Lu, Z., Nomura, K.-i., Wang, W., Kalia, R. K., Nakano, A. & Vashishta, P. (2007). Interaction of Voids and Nanoductility in Silica Glass. Phys. Rev. Lett. 99, 155506. https://doi.org/10.1103/PhysRevLett.99.155506.

25. Pradeep, N., Kim, D. I., Grobelny, J., Hawa, T., Henz, B. & Zachariah, M. R. (2007). Ductility at the nanoscale: Deformation and fracture of adhesive contacts using atomic force microscopy. Appl. Phys. Lett. 91, 203114. https://doi.org/10.1063/1.2815648.

26. Lu, Y., Huang, J. Y., Wang, C., Sun, S. & Lou, J. (2010). Cold welding of ultrathin gold nanowires. Nat. Nanotechnol. 5, 218-224. https://doi.org/10.1038/nnano.2010.4.

27. Wang, J., Fang, H., Wang, X., Chen, X., Lu, W. & Hu, W. (2017). Recent progress on localized field enhanced two-dimensional material photodetectors from ultraviolet-visible to infrared. Small 13, 1700894. https://doi.org/10.1002/smll.201700894.

28. Yuan, D., Dou, Y. H., Wu, Z. Z., Tian, Y. H., Ye, K. H., Lin, Z., Dou, S. X. & Zhang, S. Q. (2022). Atomically Thin Materials for Next-Generation Rechargeable Batteries. Chem. Rev. 122, 957-999. https://doi.org/10.1021/acs.chemrev.1c00636.

29. Wang, Y. Z., Zhang, Z. Y., Mao, Y. C. & Wang, X. D. (2020). Two-dimensional nonlayered materials for electrocatalysis. Energy Environ. Sci. 13, 3993-4016. https://doi.org/10.1039/D0EE01714K.

30. Li, S., Yang, N., Yuan, X., Liu, C., Ye, X. & Li, H. (2018). Hydrogen induced interface passivation in atomic layer deposited Al_2O_3 films and Al_2O_3/SiO_2 stacks. Mater. Sci. Semicond. Process. 83, 171-174. https://doi.org/10.1016/j.mssp.2018.04.031.

31. Lee, S. H., Bhopal, M. F., Lee, D. W. & Lee, S. H. (2018). Review of advanced hydrogen passivation for high efficient crystalline silicon solar cells. Mater. Sci. Semicond. Process. 79, 66-73. https://doi.org/10.1016/j.mssp.2018.01.019.

32. d'Agostino, R. & Flamm, D. L. (1981). Plasma etching of Si and SiO_2 in SF_6–O_2 mixtures. J. Appl. Phys. 52, 162-167. https://doi.org/10.1063/1.328468.

33. Rad, M. A., Ibrahim, K. & Mohamed, K. (2012). Atomic force microscopy investigation of surface roughness generated between SiO_2 micro-pits in CHF_3/Ar plasma. Superlattices Microstruct. 51, 597-605. https://doi.org/10.1016/j.spmi.2012.03.002.

34. Legtenberg, R., Jansen, H., de Boer, M. & Elwenspoek, M. (1995). Anisotropic reactive ion etching of silicon using $SF_6/O_2/CHF_3$ gas mixtures. J. Electrochem. Soc. 142, 2020. https://doi.org/10.1149/1.2044234.

35. Kresse, G. & Furthmüller, J. (1996). Efficiency of ab-initio total energy calculations for metals and semiconductors using a plane-wave basis set. Computational Materials Science 6, 15-50. https://doi.org/10.1016/0927-0256(96)00008-0.

36. Kresse, G. & Joubert, D. (1999). From ultrasoft pseudopotentials to the projector augmented-wave method. Physical Review B 59, 1758-1775. https://doi.org/10.1103/PhysRevB.59.1758.

37. Blöchl, P. E. (1994). Projector augmented-wave method. Physical Review B 50, 17953-17979. https://doi.org/10.1103/PhysRevB.50.17953.

38. Perdew, J. P., Burke, K. & Ernzerhof, M. (1996). Generalized Gradient Approximation Made Simple. Physical Review Letters 77, 3865-3868. https://doi.org/10.1103/PhysRevLett.77.3865.

Figure captions

Figure 1. Schematics of the silica (SiO_2) nano-welding setup and processes.

(A) Before the experiment, several silica nanospheres were first firmly attached to the edge of the copper mesh through the electrostatic force. And then, the tungsten tip was manipulated to approach silica nanosphere by using a STM holder.

(B–D) The first welding cycle was the process of welding a silica nanosphere to the W tip. Under the combined effect of gas and e-beam irradiation, the welding of silica could be realized at room temperature. In the first welding cycle, we can see that the W tip and silica nanosphere were welded together.

(E–K) The 2^{nd}, 3^{rd}, 4^{th}, 5^{th}, 6^{th}, and 7^{th} welding cycle was subsequently finished by using the same procedure.

(L–O) Silica nanospheres are welded to produce some complex 3D shapes.

Figure 2. The detailed cold welding process of silica nanospheres.

(A) Two silica nanospheres were brought into proximity before the welding.

(B–D) Under the e-beam irradiation in a no gas environment, the silica nanosphere welding process started immediately and continues to expand outward.

(E) The schematic of a self-assembled in situ TEM-AFM device for the tensile test. The target sample was first welded to the Si tip, and then welded to the tip of the AFM cantilever. We stretched the Si tip, and the welded sample moved along the same direction, meanwhile the AFM cantilever was bent. Through measuring the deflection of the AFM cantilever, we can calculate the tensile strength of the sample.

(F) A real image of the experiment setup.

(G–J) The tensile test for a welded silica nanowire, and it displayed a typical brittle fracture.

Figure 3. Effects of different atmospheres on speeding up or suspending the welding process of silica nanospheres.

(A) Under the e-beam irradiation in no gas environment, the silica nanosphere welding.

(B) Under the e-beam irradiation in a CHF_3-SF_6-O_2 environment, the silica nanosphere welding.

(C) Under the e-beam irradiation in a H_2 environment, the silica nanosphere welding. (A–C, The silica nanospheres were welded under electron beam irradiation in no gas, CHF_3-SF_6-O_2 and H_2 environments, respectively.)

(D) The enthalpies of formation of silica with a clean surface and silica after hydrogen passivation varies with the thickness of the vacuum layer.

(E) Silica energy change with different hydrogen coverage.

Figure 4. Schematic of thermal and mechanical activation mechanism on the glass nano-welding.

(A) The stress-strain curve of the load and compression of silica when the e-beam was turned off or on.

(B) The relationship between temperature reciprocal and time logarithm for different contact widths of silica nanospheres.

(C) The e-beam and surface tension effect on the thermal activation energy barrier. The e-beam

irradiation can increase the concentration of defects and further makes the thermal activation more important, and increasing surface tension force can decrease the thermal activation energy barrier.

Captions for Supplementary Videos

Video S1.

The welding process of the silica nanospheres was achieved in the ETEM chamber under e-beam irradiation. The video was recorded at 4 frames/second, and played at 25× speed.

Video S2.

Characterizing the cold welding processes for multiple times in the ETEM chamber under e-beam irradiation. The video was recorded at 4 frames/second, and played at 10× speed.

Video S3.

In situ TEM-atomic force microscopy (AFM) testing of the welded structures. Under the tensile force, the welded silica nanospheres move downwards, while the AFM cantilever was bent. According to the formula $F = K \cdot \Delta X$, we can obtain the tensile strength of the weld junction. The video was recorded at 4 frames/second, and played at 3× speed.

Video S4.

A high magnification characterization on the weld junction in different environments (including no gas, CHF_3-SF_6-O_2, and H_2). When two fresh silica nanospheres come into contact, they can be welded together. The welding speed in CHF_3-SF_6-O_2 atmosphere is faster than in no gas condition. In comparison, in H_2 environment, the two contacted silica nanospheres could not be welded together. The video was recorded at 4 frames/second, and played at 1× speed.

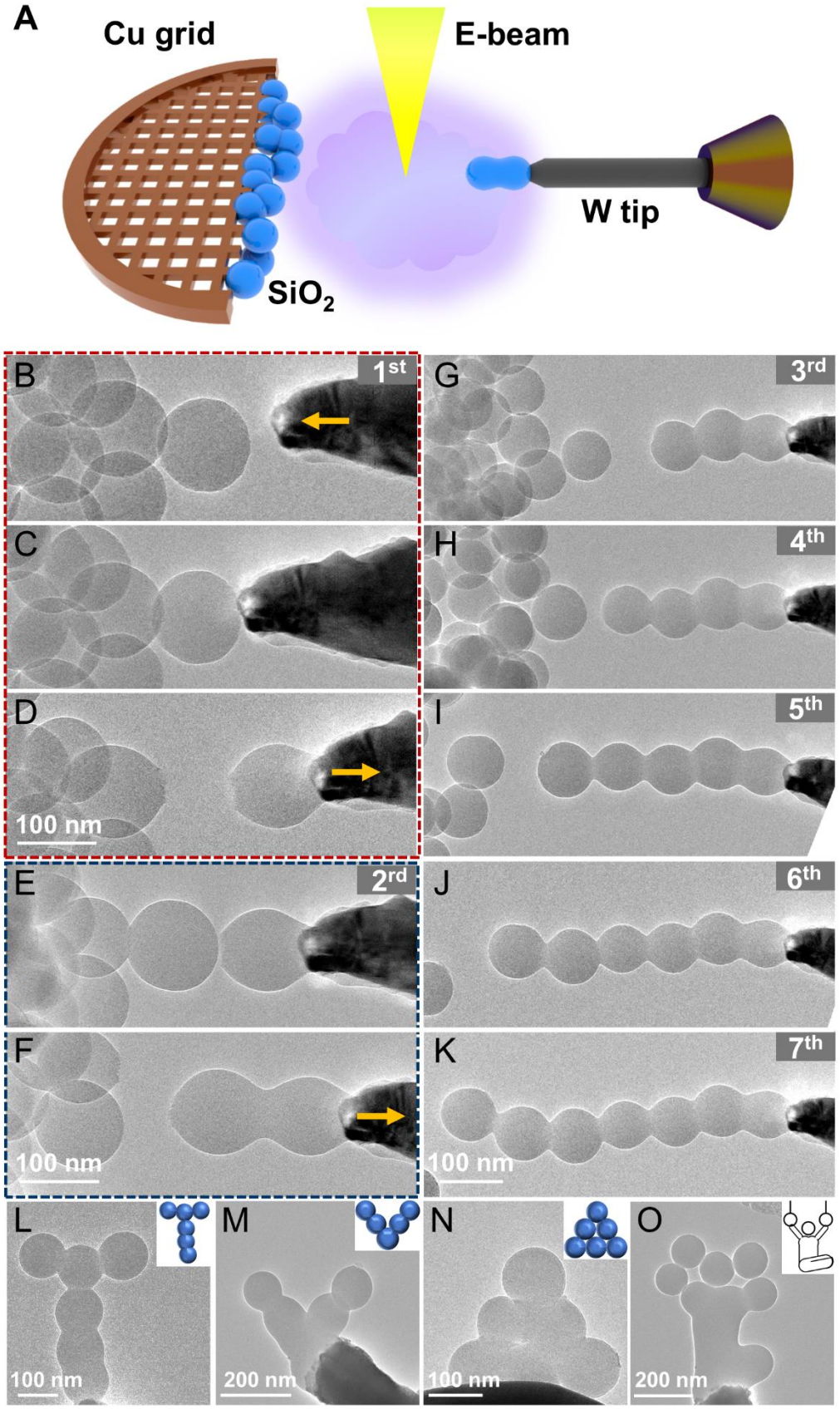
A
Cu grid
E-beam
W tip
SiO_2
B
1st
C
D
100 nm
E
2rd
F
100 nm
G
3rd
H
4th
I
5th
J
6th
K
7th
100 nm
L
100 nm
M
200 nm
N
100 nm
O
200 nm

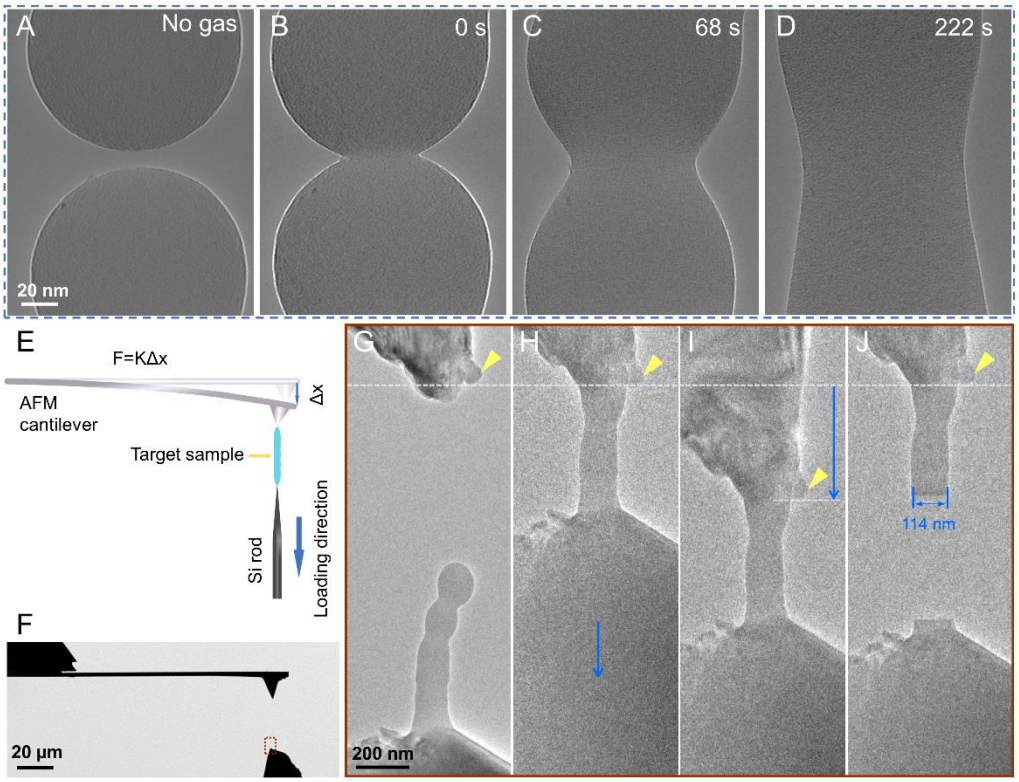
A
No gas
B
0 s
C
68 s
D
222 s
20 nm
E
F=KΔx
AFM
cantilever
Δx
Target sample
Si rod
Loading direction
F
20 μm
G
H
I
J
114 nm
200 nm

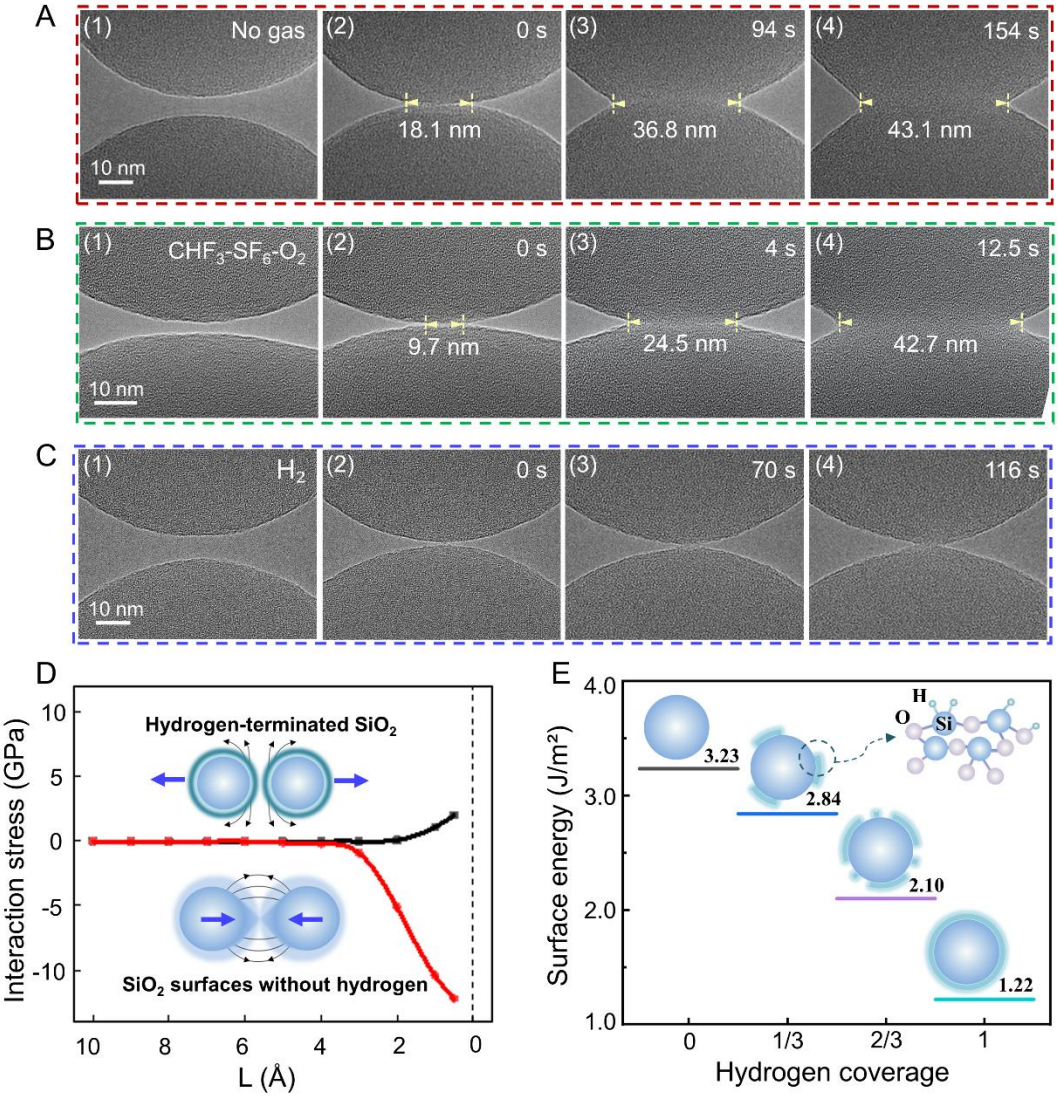
A
(1) No gas
(2) 0 s
18.1 nm
(3) 94 s
36.8 nm
(4) 154 s
43.1 nm
10 nm
B
(1) CHF3-SF6-O2
(2) 0 s
9.7 nm
(3) 4 s
24.5 nm
(4) 12.5 s
42.7 nm
10 nm
C
(1) H2
(2) 0 s
(3) 70 s
(4) 116 s
10 nm
D
Hydrogen-terminated SiO2
SiO2 surfaces without hydrogen
Interaction stress (GPa)
L (Å)
E
Surface energy (J/m²)
3.23
2.84
2.10
1.22
H
O
Si
Hydrogen coverage

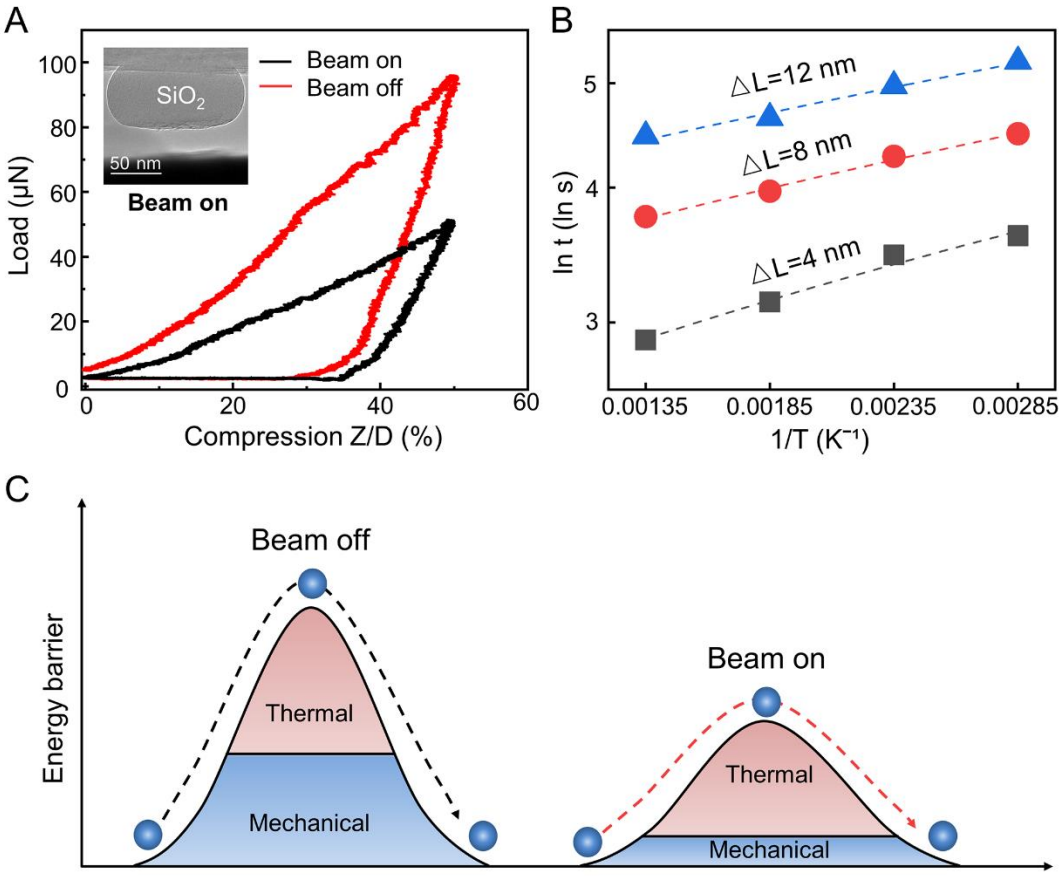
A
Load (μN)
Compression Z/D (%)
Beam on
Beam off
SiO2
50 nm
Beam on
B
ln t (ln s)
1/T (K⁻¹)
△L=12 nm
△L=8 nm
△L=4 nm
C
Energy barrier
Beam off
Thermal
Mechanical
Beam on
Thermal
Mechanical